Journal of Structural Dynamics, 1, (pp. 217-235) 2022
Computational Modeling of Nonlinear Dynamics and Its Utility in MEMS Gyroscopes

Journal of
Structural
Dynamics

Computational Modeling of Nonlinear Dynamics and Its Utility in MEMS Gyroscopes

Donghao Li *[1], Steven W. Shaw †[1,2,3], and Pavel M. Polunin ‡[2,3]

[1] *Department of Mechanical and Civil Engineering, Florida Institute of Technology, Florida 32901, USA*
[2] *Department of Mechanical Engineering, Michigan State University, Michigan 48824, USA*
[3] *Department of Physics and Astronomy, Michigan State University, Michigan 48824, USA*

Abstract

This paper describes a hybrid approach for modeling nonlinear vibrations and determining essential (normal form) coefficients that govern a reduced-order model of a structure. Incorporating both computational and analytical tools, this blended method is demonstrated by considering a micro-electro-mechanical vibrating gyroscopic rate sensor that is actuated by segmented DC electrodes. Two characterization methods are expatiated, where one is more favorable in computational tools and the other can be used in experiments. Using the reduced model, it is shown that tuning the nonuniform DC bias results in favorable changes in Duffing and mode-coupling nonlinearities which can improve the gyroscope angular rate sensitivity by two orders of magnitude.

Keywords: Vibrating ring gyroscope; MEMS; Rate sensitivity; Nonlinear vibration; Nonlinear coupling; Parametric amplification; COMSOL characterization

Received on May 10, 2021, Accepted on February 7, 2022, Published on March 4, 2022

1 Introduction

Micro-electro-mechanical systems (MEMS) are commonly used in applications including signal processing, sensing, RF switching, actuation, and timekeeping, owing to their advantages in sensitivity, high frequency range, low power consumption, and low noise [1, 2]. Because of their size, MEMS devices possess the important feature where mechanical forces and electrostatic forces are of comparable orders, an attribute not common in macroscopic electromechanical systems. Most MEMS resonators are relatively simple in their mechanical designs, typically consisting of beams, plates, or lumped masses that are lightly damped and have frequencies in the $\mathrm{kHz}-\mathrm{MHz}$ range [3]. MEMS devices offer the potential of actively exploiting a variety of nonlinear behaviors [4, 5]. For instance, a bistable potential in MEMS can be used for energy harvesting [6] and microscale mass sensing [7]. Moreover, nonlinear MEMS devices are also employed in applications including threshold pressure sensors [8], bifurcation based mass sensors [9], active switches for gas detection [10], and suppressing frequency fluctuations due to various noise sources [11]. Nonlinear mode coupling effects have also received extensive attention, with applications that include extending the ringdown time with $1:3$ internal resonance [12, 13, 14, 5], noise reduction [15, 16, 17, 18], utilizing frequency veering to realize a bandpass filter [19], and tuning vibration characteristics with a secondary resonator [20]. In order to understand and embrace the rich nonlinear behaviors in MEMS, this paper presents a hybrid approach that blends computational analysis of a finite element (FE) model [21] with the advantages offered by reduced-order models (ROM) [22]. This is achieved by distilling the pertinent information from the nonlinear FE model systems, which is used for studying the ROM. The key to connecting the two models is based on the theory of normal forms [23], which offers a rigorous guide to which model coefficients are essential, significantly simplifying the analysis. In the present work, this approach is demonstrated for a MEMS vibratory gyroscope with nonuniform electrostatic tuning. The dynamic response of interest

---

* `lid2016@my.fit.edu`
† `sshaw@fit.edu`
‡ `poluninp@msu.edu`

is described by two modes with nonlinear terms, including inter-mode coupling. The present study shows that two nonlinear coefficients, namely the (equal) Duffing nonlinearity for the modes and a single coupling coefficient, are sufficient to describe and optimize the response. This approach is similar in spirit, namely, the tailoring normal form coefficients, to that presented in [24], where shape optimization was proposed as a method for tailoring nonlinear response, which was successfully implemented for Duffing nonlinearities in MEMS [25].

MEMS vibratory gyroscopes enjoy the merits of high sensitivity to small angular rates, significant tunability, and excellent compatibility with integrated circuits [26, 27]. As a consequence, there has been a significant amount of basic and applied research related to different forms of MEMS vibratory gyroscopes, including, for example, single-structure three-axis gyroscopes [28, 29], dual-mass gyroscopes [30], vibrating ring gyroscopes (VRG) [26], and disk resonator gyroscopes (DRG) [31]. One of the pioneering works on MEMS gyroscopes is the high aspect-ratio, combined poly and single-crystal silicon (HARPSS) VRG [26], for which design, fabrication, and testing were demonstrated. In addition to the VRG, the DRG exemplifies another common type of MEMS device, featuring a larger capacitive area and a more complex mechanical structure that entails superior tunability using electrostatics [32]. For most MEMS gyroscopes, their nonlinearities are dominated by electrostatics, which have a softening effect; however, it is known that a stiffening behavior is also possible, for instance, from tether suspensions [33]. In addition, in cyclically symmetric gyroscopes with $1:1$ degenerate modes, a $1:2$ internal resonance can also be adopted in the design, providing quadratic nonlinear coupling for the rate sensor. This can be achieved in a variety of ways, such as using two coupled resonators [34], or utilizing hyperelastic materials [35]. While such relatively simple devices are not used in current applications, they are useful for testing ideas that have the potential for implementation in multi-axis gyroscopes with more complex geometries.

Ring gyroscopes consist of a thin ring suspended from a central post with soft springs and with electrodes placed around the circumference. Due to their cyclic symmetry, these rings have pairs of degenerate vibration modes [36]. One of these, the *drive mode*, is resonantly driven with one set of electrodes and the other, the *sense mode*, is used for readout using capacitive effects from another set of electrodes. These two modes are linearly coupled by Coriolis effects when the ring is subjected to rotation about the axis of symmetry, and this coupling is the basis of the device input and output characteristics [27].

Rate sensitivity, that is, the amplitude of the output signal for a given rotation rate, is an essential device characteristic of MEMS vibratory gyroscopes, and is the focus of this study. Typically, a large signal is desired in order to extract it in the presence of the inevitable background noise. Typically, the gyroscope is operated such that the response of the drive mode is linear, in order to avoid undesirable and unpredictable nonlinear effects. One important limit to the linear dynamic range of these devices is the Duffing nonlinearity of the modes, which can arise from mechanical and/or electrostatic effects. Another nonlinearity observed in gyroscopes is related to coupling of the drive and sense modes. In fact, it has been experimentally observed that self-induced parametric amplification arising from nonlinear dispersive coupling can greatly improve the system's input-output performance [37]. Furthermore, the dynamic modulation of modal coupling can be demonstrated, wherein parametric pumping is implemented, and the coupling is tuned by electrostatics [38]. Also, it has been proposed to use nonuniform DC bias voltage, variable electrode gap distance, and variable ring thickness allowing one to tailor the Duffing nonlinearity and dispersive coupling strength, which can be used to influence the rate sensitivity [39]. The analysis in [39] was based on a simplified two degree of freedom, ROM derived by modal projections of the governing PDE, as described in [40]. Of the proposed nonlinear strategies, the nonuniform DC bias tuning is the simplest to implement and forms the basis of our present work, in which we clearly demonstrate the utility and validity of the ROM by deriving its coefficients from a FE model.

Certain properties of a MEMS gyroscope are fixed by hardware, namely its mechanical form and the layout of electrodes for actuation and readout. Once these are determined, one can vary the following inputs: the drive mode excitation amplitude and frequency and, importantly, the DC biases on electrodes. The present design is based on optimizing some aspect of performance over a range of configurations and inputs. We start with a simple ring with a set of segmented electrodes that offer the desired nonuniformity, while preserving the symmetry of the modes of interest. This leads to a pattern of DC voltages with two tuning parameters, a uniform component that can be used for tuning of the operating frequency, and a nonuniform component that allows one to manipulate the Duffing and mode-coupling nonlinearities to achieve the desired response. Once the desired tuning is determined, the corresponding drive mode operating conditions are implemented, specifically, the maximum amplitude attainable without encountering bistability in the frequency response. While this is a restricted optimization problem, it demonstrates the power of tailoring nonlinearities to enhance system performance.

The selection of the nonuniform bias considers two competing effects. The Duffing nonlinearity is desired to be small so that one can operate the drive mode at a large amplitude. On the other hand, the nonlinear dispersive coupling coefficient is desired to be large in order to maximize the parametric pumping of the sense mode. As these

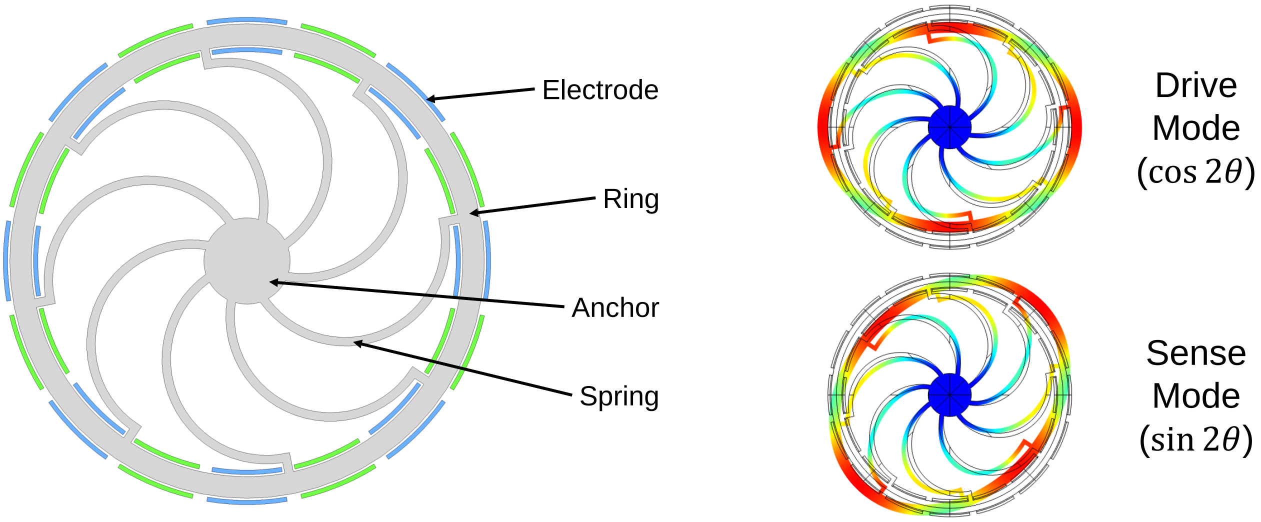

Fig. 1: Schematic diagram of the VRG with nonuniform DC bias. The gyroscope ring is modeled using the isotropic single-crystal silicon model in COMSOL. It has an inner diameter of $200\,\mu\mathrm{m}$, a width of $10\,\mu\mathrm{m}$, and an electrode gap distance of $1\,\mu\mathrm{m}$. The blue/green electrodes have a DC bias voltage of $V_{\mathrm{DC}}\,(1 \pm r_{\mathrm{DC}})$. The diagrams on the right indicate the drive and sense modes. Diagrams created using COMSOL [41]

two nonlinearities are intrinsically linked by the device physics, guided by the observations in [40], we consider how the rate sensitivity depends on a ratio of the two coefficients, resulting a relatively simple single-parameter optimization. This exhibits the utility of the fundamental understanding obtained from the ROM.

Herein, a COMSOL [41] FE model of a MEMS VRG is employed to characterize and manipulate the system parameters based on the ROM. For actuation of the gyroscope's drive mode, we consider an open-loop, externally imposed, resonant harmonic drive. [1] We use static and dynamic simulation-based setups for characterization of the gyroscope's linear and nonlinear parameters. Two methods of characterizing the essential nonlinear parameters are presented and compared, one involving a controlled static deformation and the other using a time domain simulation of the full FE model. The results demonstrate the validity of the two characterization approaches, which gives confidence to using the ROM for analyzing the response. These results are used to illustrate the significant rate sensitivity improvement offered by optimal tuning of the nonuniform DC bias.

This paper considers an highly idealized model (based on the theory of normal forms) and focuses on nonlinear phenomena, specifically,tuning the nonlinear dynamics of a vibratory MEMS gyroscope to enhance its sensitivity. It is recognized that there are many critical practical issues related to gyroscope design and dynamics that are not considered in the present work, such as quadrature error, mode matching, material and damping anisotropy, nonideal electrostatic effects, temperature and other environmental sensitivities, resolution, bandwidth, etc., cf. [27]. The ultimate utility of the presented approach for nonlinear tuning will rely on its capacity to mesh with the techniques used to address these other effects.

This paper is organized as follows. In Section 2, we present the basic description of the COMSOL FE model and the essential two-mode vibration model and describe the process of deriving the former from the latter. In Section 3, we describe and compare the two characterization methods for identification of nonlinear system parameters. In Section 4, we analyze the results from the COMSOL model and numerical simulations of the ROM while varying the pattern of DC tuning, and we determine its implications for optimizing the rate sensitivity. Finally, conclusions are drawn in Section 5.

2 Modeling

This section describes the main features of the computational and reduced-order models and the means of distilling the latter from the former.

---

[1] In practice, closed loop operation employing a phase-locked loop is used, but this is equivalent to the open-loop drive response in terms of the form of the frequency response.

2.1 Layout and FE Model

In this work, a prototypical model for a VRG under electrostatic actuation and sensing is created and analyzed using COMSOL Multiphysics [41]. The basic layout for the device is shown in Fig. 1. The ring, representing the main portion of the gyroscope proof mass, is suspended by eight semi-circular arcs, which act as curved support springs and are attached to a central anchor. The ring inner diameter is chosen to be $200\,\mu\mathrm{m}$ and its width is $10\,\mu\mathrm{m}$. In our simulations we chose the ring material to be single-crystal silicon, which is taken to be uniform and isotropic with an effective elastic modulus and Poisson's ratio.[2] The vibrations of interest occur in plane and therefore a planar FE model is employed. This assumption is reasonable due to the high aspect ratio of the structure. Also, since we are modeling a rotation rate sensor, in COMSOL we impose a global rotation rate of Ω to the frame of reference in which the structure vibrates.

For operation as a rate gyroscope, the lowest frequency pair of degenerate modes are of interest: the drive mode, with a mode shape having azimuthal dependence $\cos 2\theta$, and the sense mode, with a mode shape of $\sin 2\theta$. These two modes maintain a 45° difference in their nodal diameters and are conveniently addressed by the chosen electrode pattern [26]. The segmented electrodes are used to approximate these modes in an azimuthally discrete manner, in order to access them independently.

One of the main goals of the present study is to examine the effects of a nonuniform pattern of DC bias voltages on the system response. To that end, we generalize the system so that the DC bias is nonuniform on the electrodes, in the pattern indicated in Fig. 1. Specifically, there are 32 cyclically arranged, segmented electrodes, 16 of which are evenly positioned on the periphery of the ring, and 16 others are located on its interior, hence preserving the cyclic symmetry of the system at the order of the vibration modes of interest, namely, those with two nodal diameters [36]. As we elaborate below, the presence of electrodes on both the interior and exterior sides of the ring helps to minimize coupling of the drive/sense modes to other vibrational modes. The electrostatic gap between the ring and electrodes are chosen to be $1\,\mu\mathrm{m}$, which is similar to the typical gap dimensions obtained in microfabrication processes [42]. The number of electrodes is chosen deliberately in order to study the effect of nonuniform bias voltage on the dynamical performance of the gyroscope. As shown in previous work [39], an 8-electrode (accounting for exterior electrodes only) configuration can support only a uniform bias distribution necessary for preserving mode matching of the drive and sense modes, and the minimal number of exterior electrodes that can support a nonuniform bias is 16. Nonuniformity of the DC bias is implemented by applying two distinct voltages to adjacent electrodes. In particular, the electrodes have DC bias voltages of $V_{\mathrm{DC}}\,(1 \pm r_{\mathrm{DC}})$, where $+$ $(-)$ is applied for even- (odd-) numbered electrodes, as depicted by the blue and green electrodes in Fig. 1. Due to the selection of the drive and sense modes, the sign of r_{DC} matters. Typically, the range for r_{DC} is $[-1, 1]$.

VRGs possess many vibration modes, encompassing torsional, radial, translational, flexural, and out of plane modes, some of which are depicted in Table 1 (these modes are described in more detail below). All modes except the drive and sense modes, modes 4 and 5 in Table 1, are considered extraneous to its function, but nonlinearities will necessarily couple all modes to some degree. Also, although the system is constructed with cyclic symmetry in COMSOL, we allow for asymmetric responses, for example, arising from the coupling of the modes of interest to these extraneous modes. These other modes can render the dynamics of the drive and sense modes to be effectively noisy. This is especially the case since these devices are lightly damped, and these intermodal interactions are widely observed in COMSOL simulations. Of course, such noisy responses are associated with loss of signal resolution and increased dissipation of the modes of interest. In contrast with previous VRG designs, where only the outer electrodes are employed, this design embraces the inner electrodes, as these were found to help restrain unfavorable couplings to other modes.

2.2 Two-Mode Model

In this section we briefly review the essential features of gyroscope operation, which can be described by a two-mode model for the drive and sense modes. For the present work, this model must include nonlinear effects which, as will be demonstrated, are dominated by electrostatic effects.

The operation of a VRG, or any single-axis gyroscope, is based on Coriolis coupling of the drive and sense modes, which is linear in terms of the modal velocities. Simple linear vibration models with two modes are able to capture the basic operational aspects of such gyroscopes, but nonlinear effects can play an important role. The nonlinearities of present interest are captured in a potential comprising the drive and sense mode amplitudes, incorporating both

---

[2] In COMSOL, an option for isotropy is provided for single crystal silicon, which makes the (qualitative) material properties very similar to polysilicon, with slight differences in the values of the material constants. Therefore, we note that discrepancies may exist between our analysis and single crystal silicon models of MEMS gyroscopes.

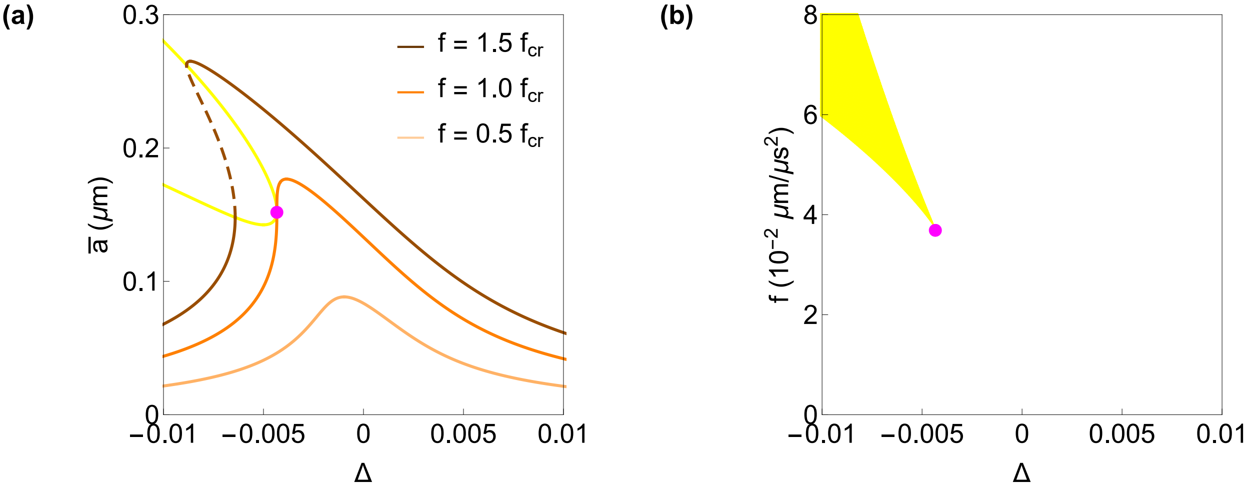

Fig. 2: Drive mode steady-state response. **(a)** Drive mode steady-state amplitude versus frequency detuning parameter, with $f = f_{\mathrm{cr}}$ and with back-action from the sense mode neglected. The orange curves demonstrate the frequency response at different drive levels, where the solid curves suggest stable responses, and the dashed curves are for unstable responses. The yellow curve signifies the saddle-node (SN) bifurcation conditions, and the magenta dot represents the critical condition. **(b)** Parameter plane for drive amplitude versus drive frequency. The yellow region indicates the bistability region. which is bounded by the SN conditions. The magenta dot manifests that the critical condition is also the cusp bifurcation condition where the SN conditions meet

individual mode Duffing (cubic) nonlinearities and dispersive intermodal coupling [40]. The entire potential is thus given by

$$U = \frac{1}{2}\left(\omega_4^2 A^2 + \omega_5^2 B^2\right) + \frac{1}{4}\left(\gamma_4 A^4 + \gamma_5 B^4\right) + \frac{1}{2}\kappa A^2 B^2, \tag{1}$$

where A and B represent the drive and sense modal displacements respectively, ω_4 and ω_5 denote their eigenfrequencies respectively, γ_4 and γ_5 describe their Duffing coefficients respectively, κ indicates the dispersive coupling strength, and the modal masses are normalized to unity. Due to cyclic symmetry, the modes have equal coefficients and we thus define $\omega_0 = \omega_4 = \omega_5$ and $\gamma = \gamma_4 = \gamma_5$. The parameters in the potential, which involve both mechanical and electrostatic effects [40], are to be characterized for the FE model by COMSOL, as subsequently elaborated in Sect. 3.

With these terms, a two-mode nonlinear ROM captures the essential system dynamics of interest and, after it is validated with COMSOL, it will be employed for analysis and numerical simulations to determine the gyroscope input-output gain. To derive the equations of motion, the kinetic energy is taken to be simply $T = \dot{A}^2/2 + \dot{B}^2/2$ and the Lagrangian approach is employed. Also included in the model are linear dissipation, resonant harmonic forcing applied to the drive mode, and the Coriolis coupling [40]. Putting these terms together, the ROM dynamics are governed by

$$\ddot{A} + 2\zeta\omega_0\dot{A} + \omega_0^2 A + \gamma A^3 + \kappa A B^2 = \nu\Omega\dot{B} + f\cos\omega t, \tag{2}$$

$$\ddot{B} + 2\zeta\omega_0\dot{B} + \omega_0^2 B + \gamma B^3 + \kappa A^2 B = -\nu\Omega\dot{A}, \tag{3}$$

where ζ represents the modal damping ratio (assumed to be the same for both modes), Ω dictates the angular rate of the gyroscope (the quantity to be measured), f indicates the direct drive amplitude, ω specifies the drive frequency, which is near ω_0, and the coefficient ν captures the Coriolis coupling strength ($\nu = 8/5$ for a thin ring gyroscope [40]). The amplitudes of the time-dependent quantities A and B are denoted by a and b respectively, and a nondimensional frequency detuning parameter is defined as $\Delta = \omega/\omega_0 - 1$.

In these systems, the drive mode is maintained at some fixed amplitude and the Coriolis coupling generates a signal in the sense mode under rotation. In the present work, nonlinear mode coupling is used to amplify the Coriolis coupling via parametric amplification [43, 44, 37, 40]. For realistic operating conditions, the sense mode amplitude is much smaller than the drive mode amplitude. Thus, for the drive mode, the back-action from the sense mode is assumed to be negligible due to its relatively small amplitude [40], in which case the terms associated with κ and $\nu\Omega$ in Eq. (2) may be ignored. This assumption results in one-way coupling from the drive to the sense mode, and is justified by the FE simulation results.

Fig. 2 shows the steady-state operating condition of the drive mode, where the back-action from the sense mode is assumed to be negligible. These response curves are obtained from the numerical simulations of the two-mode ROM. Using the stated assumption, the critical operating condition for the drive mode can be directly obtained from the cusp bifurcation condition of a simple Duffing oscillator using the method of averaging [23]. This condition, which provides the largest drive mode signal possible without inducing bistability, has excitation amplitude and frequency expressed as [45]

$$f_{\mathrm{cr}} = \frac{16\omega_0^3}{3}\sqrt{\frac{\zeta^3}{\sqrt{3}\,|\gamma|}}, \tag{4}$$

$$\omega_{\mathrm{cr}} = \omega_0 + \sqrt{3}\zeta\omega_0 \mathrm{sgn}(\gamma), \quad \text{or} \quad \Delta_{\mathrm{cr}} = \sqrt{3}\zeta \mathrm{sgn}(\gamma), \tag{5}$$

This yields the critical drive mode amplitude

$$\bar{a}_{\mathrm{cr}} = 4\omega_0\sqrt{\frac{\zeta}{3\sqrt{3}\,|\gamma|}}, \tag{6}$$

which is treated as the maximum allowable vibration amplitude of the drive mode. This ensures a monostable frequency response, i.e., it operates in its linear dynamic range, which is inherently limited by the Duffing nonlinearity γ. The plots in Fig. 2 use the characterization results given in Sect. 4.1 with $\zeta = 0.0025$ (equivalent to a quality factor of $Q = 200$) which yields $f_{\mathrm{cr}} = 0.0372\,\mu\mathrm{m}/\mu\mathrm{s}^2$ and $\omega_{\mathrm{cr}}/(2\pi) = 1.03\,\mathrm{MHz}$, or, equivalently $\Delta_{\mathrm{cr}} = -0.00433$.

In applications, instead of an imposed harmonic drive, such systems are typically driven using a feedback loop with an amplifier and a phase locked loop (PLL). In this case, the open-loop direct drive term $f\cos\omega t$ in Eq. (2) is replaced by a closed-loop term $f\cos[\omega_0 t + \phi(t) + \delta]$, where ϕ defines the phase of the drive mode response relative to its input, and δ represents an imposed phase shift. By varying the phase shift δ from 0 to π, the PLL produces the same frequency response as the open-loop system except for the fact that unstable portion of the response (see dashed curve on Fig. 2a) becomes stable. This gives an advantage that the unstable branch (as in an open loop system) is also measurable in experiments [46, 47]. For the Duffing drive mode model using closed loop operation, that is, with a PLL, the method of averaging can also be used [48], allowing one to determine its steady-state frequency and amplitude. This yields the closed loop frequency response in terms of the parametric equations

$$\omega = (1 - \zeta\cot\delta)\,\omega_0 + \frac{3\gamma f^2\sin^2\delta}{32\zeta^2\omega_0^5}, \tag{7}$$

$$\bar{a} = \frac{f\sin\delta}{2\zeta\omega_0^2}. \tag{8}$$

At the critical condition, the above equations coincide with Eqs. (5)–(6).

The sense mode amplitude of the gyroscope provides the desired information about the rotation rate Ω. The gyroscope input-output gain is a crucial measure of performance, taken here to be the rate sensitivity S, defined to be the ratio of the amplitude of the output (sense mode) signal normalized by the rotation rate (the input). We assume a constant rotation rate Ω and steady state operation of the drive and sense modes. We also assume that the drive mode is operating at its critical condition with amplitude $\bar{a}_{\mathrm{cr}}$, resulting in a sense mode amplitude of $\bar{b}$, for which the sensitivity is expressed as [39, 40]

$$S = \left.\frac{\bar{b}}{\Omega}\right|_{\bar{a}=\bar{a}_{\mathrm{cr}}}. \tag{9}$$

To improve the rate sensitivity, the gyroscope gain is enhanced by increasing $\bar{b}$ for a given Ω using two effects that are governed by system nonlinearities: (i) extending the linear dynamic range of the drive mode and (ii) parametric amplification of the sense mode which originates from inter-mode dispersive coupling that is inherent in the system.

In normal operation the sense mode amplitude b is much smaller than the drive mode amplitude a. This is verified for our model using numerical simulations based on the results obtained in Sect. 4. In the drive mode, the A^3 term limits the range of the amplitude a, since the drive mode should not experience bistability. Therefore, it is desirable to reduce the Duffing coefficient γ of the drive mode in order for it to operate at large amplitude, thereby increasing the Coriolis coupling effect by maximizing the driving term on the sense mode, $\nu\Omega\dot{A}$ in Eq. 3. In the sense mode, this Coriolis term serves as its direct excitation, and the $\kappa A^2 B$ term, which stems from dispersive coupling with the drive mode, has an oscillating component at near $2\omega_0$ and is thus able to produce a parametric pumping effect that can amplify b. Thus, the dispersive coupling coefficient κ should be increased. (A more detailed elucidation of the parametric amplification can be found in Appendix A.) These two effects are both nonlinear and are linked to the physics of the device, and the complete dynamics must be considered in order to achieve the optimal effect on S. It is important to note that the two coefficients of interest are both contained in the potential, which incorporates both elastic and electrostatic sources, and this allows for a relatively simple characterization approach employing static deformations, which is corroborated with dynamic simulations, both using COMSOL, as shown in Sect. 4.

2.3 Derivation of ROM Coefficients From the FE Model

Modal projections are used to distill from the FE model the model coefficients that describe the coupled dynamics of the drive and sense modes. To this end, it is important to note that we assume the nonlinear effects are relatively weak, so that the drive and sense eigenmodes remain valid descriptors of the dynamics of interest. The displacement of a given mode is determined using the projection of nodal displacements onto the mode of interest. In COMSOL, this calculation can be accomplished with a line integration function. In particular, a circular path is constructed along the center of the undeformed ring, where each point on the path has a coordinate (x, y) and an attendant spatial displacement (u, v). We take θ to be the circumferential angle measured around the ring and denote $q_n(t)$ as the time-dependent anti-node displacement of mode n. Hence, the projection onto the nth mode allows one to obtain the modal amplitude by the integral

$$q_n(t) = c_n \int_0^{2\pi} \left(u(\theta,t), v(\theta,t)\right)^{\mathrm{T}} \bullet \boldsymbol{\varphi}_n(\theta)\, d\theta, \tag{10}$$

where

$$c_n = \frac{1}{\int_0^{2\pi} \boldsymbol{\varphi}_n^2(\theta)\, d\theta} \tag{11}$$

is a normalizing coefficient and $\boldsymbol{\varphi}_n(\theta)$ is the vectorized eigenfunction.

Some selected modes of interest are depicted in Table 1, which indicates the mode types, the attendant $\boldsymbol{\varphi}_n(\theta)$, their eigenfrequencies, and illustrations of the mode configurations. In order to determine the displacement for a mode of interest, Eq. (10) is used, wherein the angle θ is related to the COMSOL x and y coordinates by

$$\theta = \begin{cases} \tan^{-1}\frac{y}{x}, & x \geq 0 \\ \tan^{-1}\frac{y}{x} + \pi, & x < 0 \end{cases} . \tag{12}$$

As a consequence, the trigonometric terms in the integrand of Eq. (10) that stem from $\boldsymbol{\varphi}_n(\theta)$, are evaluated using the expressions shown in Table 1, and are given as

$$(\cos k\theta)^{m_k} (\sin l\theta)^{n_l} = \left[\cos\left(k\tan^{-1}\frac{y}{x}\right)\right]^{m_k} \left[\sin\left(l\tan^{-1}\frac{y}{x}\right)\right]^{n_l} \left[\operatorname{sgn}(x)\right]^{km_k + ln_l}, \tag{13}$$

where k, l, m_k, and n_l are nonnegative integers related to the harmonic orders of the modes and their powers. This relationship allows for adopting the appropriate signs for the integrand in Eq. (10), so that the integral can be evaluated correctly.

3 Characterization Methods

While COMSOL can readily determine the eigenfrequencies and eigenmodes of a system, coefficients for the ROM nonlinearities cannot be obtained directly from the software. Therefore, two methods of characterizing from the FE model the two essential nonlinear parameters for the ROM, γ and κ, are elaborated in this section. One method uses

Table 1: Summary of the Gyroscope Modes

n	Eigenmode	Vectorized eigenfunction $\boldsymbol{\varphi}_n(\theta)$	Eigenfrequency $\omega_n/(2\pi)$	Mode shape
1	torsional modes	$\begin{pmatrix} -\sin\theta \\ \cos\theta \end{pmatrix}$	0.351 MHz	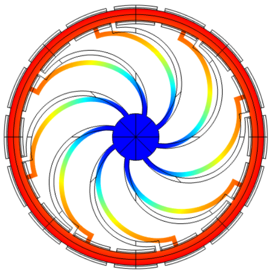
2	x translational mode	$\begin{pmatrix} 1 \\ 0 \end{pmatrix}$	0.437 MHz	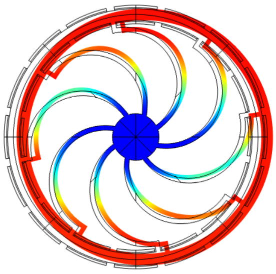
3	y translational mode	$\begin{pmatrix} 0 \\ 1 \end{pmatrix}$	0.437 MHz	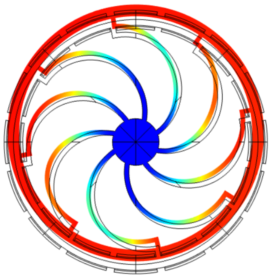
4	$\cos 2\theta$ mode (drive mode)	$\begin{pmatrix} \cos 2\theta\cos\theta \\ \cos 2\theta\sin\theta \end{pmatrix}$	1.033 MHz	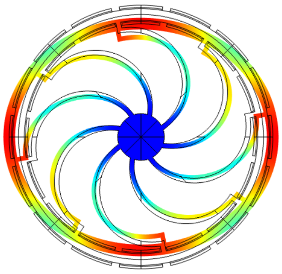
5	$\sin 2\theta$ mode (sense mode)	$\begin{pmatrix} \sin 2\theta\cos\theta \\ \sin 2\theta\sin\theta \end{pmatrix}$	1.033 MHz	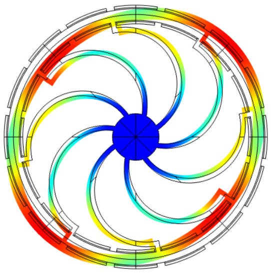

static deflection and the other uses the damped free vibration response, i.e., ringdown. The results derived from these two approaches are compared in Sect. 4.1. The characterized coefficients are then used in the ROM in order to evaluate the rate sensitivity.

For the following two subsections, the characterization procedures for determining γ and κ are carried out for the unforced $(f = 0)$ and nonrotating $(\Omega = 0)$ system, since these are device parameters that are not affected by the drive mode input or the rotation. Due to their cyclic symmetry, the eigenfrequencies $\omega_0 = \omega_{4,5}$ and the Duffing coefficients $\gamma = \gamma_{4,5}$ are equal for the drive and sense modes (and for other pairs of degenerate modes [36]). Also, due to this symmetry, although not as obvious, is the fact that for a VRG (and possibly more generally) the dispersive coupling strength κ between these modes is equal to γ [40]. As described above, the use of the proposed arrangement of electrodes conveniently preserves this symmetry. Accordingly, characterizing these parameters for only the drive mode and its coupling to the sense mode are sufficient to obtain the necessary model coefficients.

In COMSOL, the triangular element type is selected for meshing, where cyclic symmetry is imposed as mentioned above. As for the solver configurations, the linear solver is chosen to be direct, and the nonlinear solver is chosen to to fully coupled. Additionally, for the time-dependent solver (for the ringdown characterization only), the method of backward differentiation formula (BDF) is employed, and the time stepping is taken to be constant since the ringdown frequency is close to the eigenfrequency. The ensuing fitting is carried out in Mathematica to fit the acquired data to the polynomials of the desired forms (indicated by Eqs. (15)–(16) and Eqs. (17)–(18) respectively), where the fitting method minimizes the L^2 norm of the numerical difference. We next describe the two characterization methods and subsequently show and compare the obtained results.

3.1 Characterization Using Static Deflection

Measuring the deflection of the gyroscope ring under a varying static load is an expeditious approach to characterizing the parameters in the potential required for the ROM. There have been several works that utilize static loads to study nonlinear stiffness, [49, 50, 51], for instance, by employing the implicit condensation method [52]. In this work, this method involves exerting, in the FE model, an external load along the circumference of the ring with a desired azimuthal dependence, resulting in a static deflection of the ring that is very close to the desired mode shape. This approach is very simple in FE analysis and may be possible to realize in experiments. The coefficients are measured by comparing the measured deflection, as projected onto the mode of interest (the drive mode), to that predicted by the potential for the ROM. To capture nonlinear effects, the ring must be distorted such that leading order nonlinear stiffness effects are measurable. To make the ring deflect as intended, the applied load per unit radian along the circumference is expressed as

$$\boldsymbol{w}(\theta) = w\boldsymbol{\varphi}(\theta), \tag{14}$$

where w is the magnitude of the modal load applied to the drive mode in the following discussion, namely $w = c_4 \int \boldsymbol{w}(\theta) \bullet \boldsymbol{\varphi}_4(\theta)\, d\theta$ where $\boldsymbol{\varphi}(\theta)$ describes the pattern of the applied load, which is taken to be the drive mode shape. It is also known from Eq. (1) that the normalized force associated with the drive mode can be expressed as $\partial U/\partial A = \omega_0^2 A + \gamma A^3 + \kappa A B^2$. Because the modal mass has been normalized to unity in the ROM, the eigenfrequency squared can be used to represent the linear stiffness. To obtain the static displacement measurements, a parametric sweep of w is conducted by varying the magnitude of the DC bias force. The range of w is restricted so as to preclude higher-order nonlinear effects so that the cubic nonlinearities in the stiffness provide an accurate fit. Under this condition, pull-in (electrostatic buckling) is also prevented. Curve fitting is applied to the resulting load-displacement data in order to determine the Duffing and dispersive coupling coefficients. These curves are well fitted to an equation with linear and cubic stiffnesses. The linear part matches the independently obtained eigenfrequency and the cubic part yields the nonlinear coefficient of interest. This is carried out for different levels of nonuniformity in the bias.

To characterize the Duffing coefficient γ, the pattern is given by $\boldsymbol{\varphi}(\theta) = \boldsymbol{\varphi}_4(\theta)$ so the displacement of the sense mode is kept at $B = 0$, which yields the modal load as a function of the drive mode displacement

$$w|_{B=0} = \omega_0^2 A + \gamma A^3, \tag{15}$$

In COMSOL, the external load has the dimension of force per unit area, and therefore the modal load w is directly proportional to the external load. Additionally, since ω_0 is known, either from COMSOL's prestressed eigenfrequency study or from COMSOL's time dependent study for a free vibration near zero amplitude, the Duffing coefficient γ can thus be determined from the curve fit.

In a similar fashion, to characterize the dispersive coupling strength κ, the force pattern is given by $\boldsymbol{\varphi}(\theta) = \boldsymbol{\varphi}_4(\theta) + \boldsymbol{\varphi}_5(\theta)$ so that the displacement of the sense mode is maintained at $B = A$, which yields

$$w|_{B=A} = \omega_0^2 A + (\gamma + \kappa) A^3. \tag{16}$$

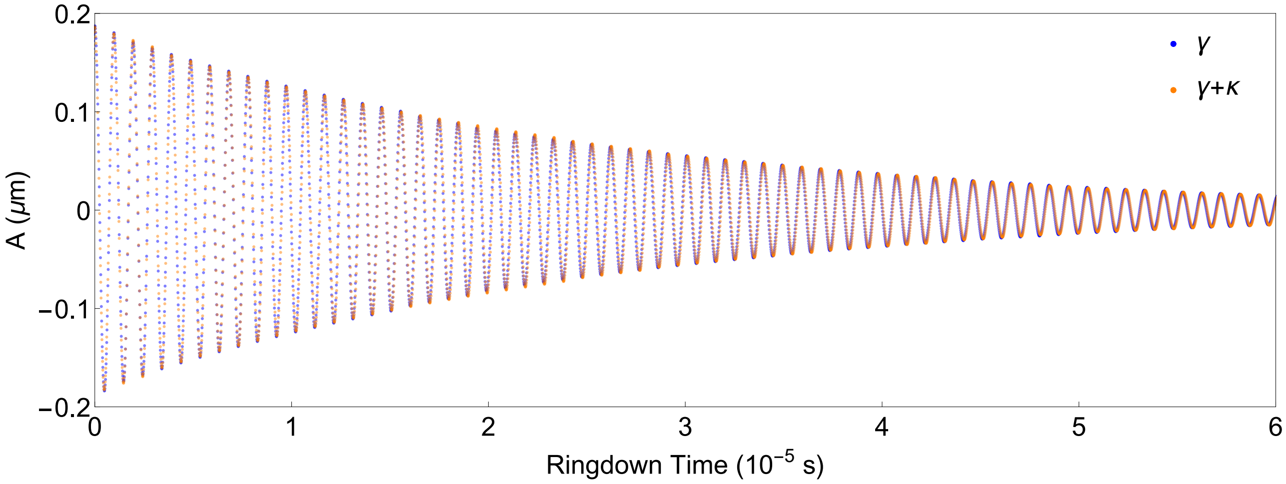

Fig. 3: Drive mode displacement versus time for characterization using a dynamic ringdown response, with $r_{\mathrm{DC}} = 0$ and $V_{\mathrm{DC}} = 150\,\mathrm{V}$. The blue data points indicate the purely Duffing response with $B(t) = 0$, and the orange data points indicate the response with dispersive coupling and Duffing, that is, $B(t) = A(t)$. Note the slight frequency difference evident as time grows, which is due to the differing nonlinear frequency shifts between γ and $\gamma + \kappa$. This shift is small for both cases, but can have a dramatic effect on the system behavior

Since both ω_0 and γ have been previously determined, the dispersive coupling strength κ can be found from the curve fit. Note that for the VRG with uniform DC bias, the system with $B = A$ has an effective Duffing coefficient that is simply double that of one of the isolated modes.

It is recognized that in a physical device the coupled mode behavior is affected by many factors, including dynamic effects not considered in this static approach. However, the approach provides baseline values for the nonlinear stiffness and coupling parameters that can be used as a starting point for more refined device tuning that will account for unmodeled effects. The static approach is straightforward and not computationally demanding. Its utility for describing dynamic behavior is considered by comparing its results with the ringdown simulations, which are described next.

3.2 Characterization Using the Ringdown Response

The ringdown response is a commonly used experimental method to characterize an oscillator's system parameters, namely the system damping ratio, eigenfrequency, and nonlinearities [53, 54]. This characterization method is based on the fact that system relaxes from its initial state to thermal equilibrium along the backbone curve of the mode of interest, that is, along the path that specifies the amplitude-dependent (nonlinear) natural frequency, which is dictated by nonlinear stiffness. The measurements are taken while the oscillator decays from a specified initial condition–typically obtained from a steady state under an external drive that is switched off–and undergoes free decay in a nearly single mode response. When the decay rate is small compared to the natural frequency, the backbone curve is followed quite closely [53].

This approach is applied to COMSOL simulations in this work, where the gyroscope ring is driven to an intended initial condition, after which the AC drive is switched off, and the ringdown is captured by acquiring the time-domain data. The characterization for both the Duffing coefficient γ and dispersive coupling strength κ are carried out under zero rotation rate ($\Omega = 0$) with a damping ratio $\zeta = 0.0025$ (equivalent to a Q factor of 200) for each mode.

In a MEMS vibratory gyroscope, such a ringdown measurement is complicated by the fact that the two modes have identical frequencies and are dispersively coupled. The actual situation in measurements is additionally subtle due to the fact that the phase difference between the two modes can dramatically impact the transient dynamics, which typically involves beating type responses and requires special treatment [55]. Therefore, the derivation for a special condition, one achievable in COMSOL, is presented in Appendix B, namely, the condition $B(t) = \beta A(t)$, where β is a constant. This assumption, on which the theory is based, allows a strategy analogous to that described in Sect. 3.1 to be adopted. By examining the ROM Eqs. (2)–(3), two properties of the dynamics during the ringdown response become manifest: (i) if the system has an initial condition of $B(t_0) = 0$ and $\dot{B}(t_0) = 0$, then $\forall\ t > t_0$, the sense mode remains at $B(t) = 0$ (that is, the drive mode is invariant, even in the nonlinear case [54, 56], as is the sense mode); (ii) if the system has an initial condition of $B(t_0) = A(t_0)$ and $\dot{B}(t_0) = \dot{A}(t_0)$, then $\forall\ t > t_0$, the equality $B(t) = A(t)$ persists (that is, the plane $B = A$ is also invariant). These two cases correspond to $\beta = 0$ and $\beta = 1$ respectively. While the ROM predicts these invariances, COMSOL simulations will, of course, involve coupling between many modes due to imperfections. However, it is shown that these properties of the ROM are largely preserved in COMSOL. Note that in experiments, parasitic coupling may not allow for such a clean ringdown signal [55].

To characterize the eigenfrequency and the Duffing coefficient γ using ringdown, the drive mode is excited by applying a harmonic AC voltage on the drive electrodes, in addition to the DC bias voltage, with the drive frequency near the natural frequency. The driven response is allowed to reach steady-state at an amplitude adequate to observe nonlinear effects, while the sense mode naturally stays at zero amplitude (or nearly so). This ensures $B(t) \approx 0$ during the ringdown response. The COMSOL response, projected onto the drive mode as it decays along the backbone curve, is compared with the amplitude-dependent natural frequency as a function of the drive mode amplitude obtained for the ROM, namely,

$$\omega_{0,\mathrm{NL}}\big|_{B(t)=0} = \omega_0 + \frac{3\gamma}{8\omega_0}a^2. \tag{17}$$

This comparison allows one to determine both ω_0 and γ from a curve fit.

To characterize the dispersive coupling strength κ, the drive and sense modes are driven by identical AC drives to adequate (equal) amplitudes, after which both AC drives are simultaneously turned off. This ensures $B(t) \approx A(t)$ during the ringdown response. By comparing the resulting ringdown measurement with the following expression for the backbone curve for the ROM,

$$\omega_{0,\mathrm{NL}}\big|_{B(t)=A(t)} = \omega_0 + \frac{3(\gamma + \kappa)}{8\omega_0}a^2, \tag{18}$$

one can use curve fitting to determine κ, since ω_0 and γ have been previously determined.

A sample plot of a ringdown response for the $r_{\mathrm{DC}} = 0$ case is shown in Fig. 3, from which the nonlinear coefficients can be obtained. Specifically, the frequency data is obtained by finding the zero-crossing points of the displacement using linear interpolation; this also assists in acquiring the amplitude data, which lie half-way between the zero-crossing points. Fig. 3 illustrates that the two ringdown responses correspond to slightly different amplitude-dependent natural frequencies, which stems from the fact that the system evolves along two distinct backbone curves, as shown in detail in the next section. While these nonlinear effects appear to be quite small in this Figure, they are evident on a backbone curve, as shown in the next section, and, most importantly, their effects on the system response are significant, as subsequently demonstrated.

These two approaches are next used to characterize the nonlinear coefficients of the system and their dependence on the tuning of the nonuniformity of the DC bias. This dependence is used to determine a tuning that optimizes the gyroscope sensitivity.

4 Results

There are two main groups of results described in this section. The first relates to the COMSOL device characterization results as a function of the bias nonuniformity tuning parameter r_{DC}, which provides confidence for the second, and main, results of the paper, namely, the improvement in the device sensitivity achieved by tailoring the nonlinear coefficients in the ROM using nonuniform DC bias.

4.1 Characterization Results

Fig. 4 shows a summary of the characterization results obtained using COMSOL. The system parameters of primary interest characterized by COMSOL are the eigenfrequencies, the Duffing and dispersive nonlinear coefficients, their dependence on the rotation rate Ω, and their dependence on the DC bias and its nonuniformity. Since the eigenfrequencies of various modes can be tuned by electrostatics, it is important to determine how they depend on the uniform part of the DC bias voltage. Fig. 4a illustrates that increasing the level of a uniform DC bias reduces the eigenfrequencies of the 2θ modes (as expected, since electrostatic effects are softening), has no effect on the torsional modes (as expected), and softens the translational modes, even to the point of buckling. Moreover, changes in the angular rate engender splittings in the eigenfrequencies of the degenerate modes, as expected and as displayed in Fig. 4b. However, for rotation rates relevant to applications–usually on the order of $1\,\mathrm{Hz}$–such separation is regarded as inconsequential. since they are well below those expected due to imperfections arising from finite fabrication tolerances.

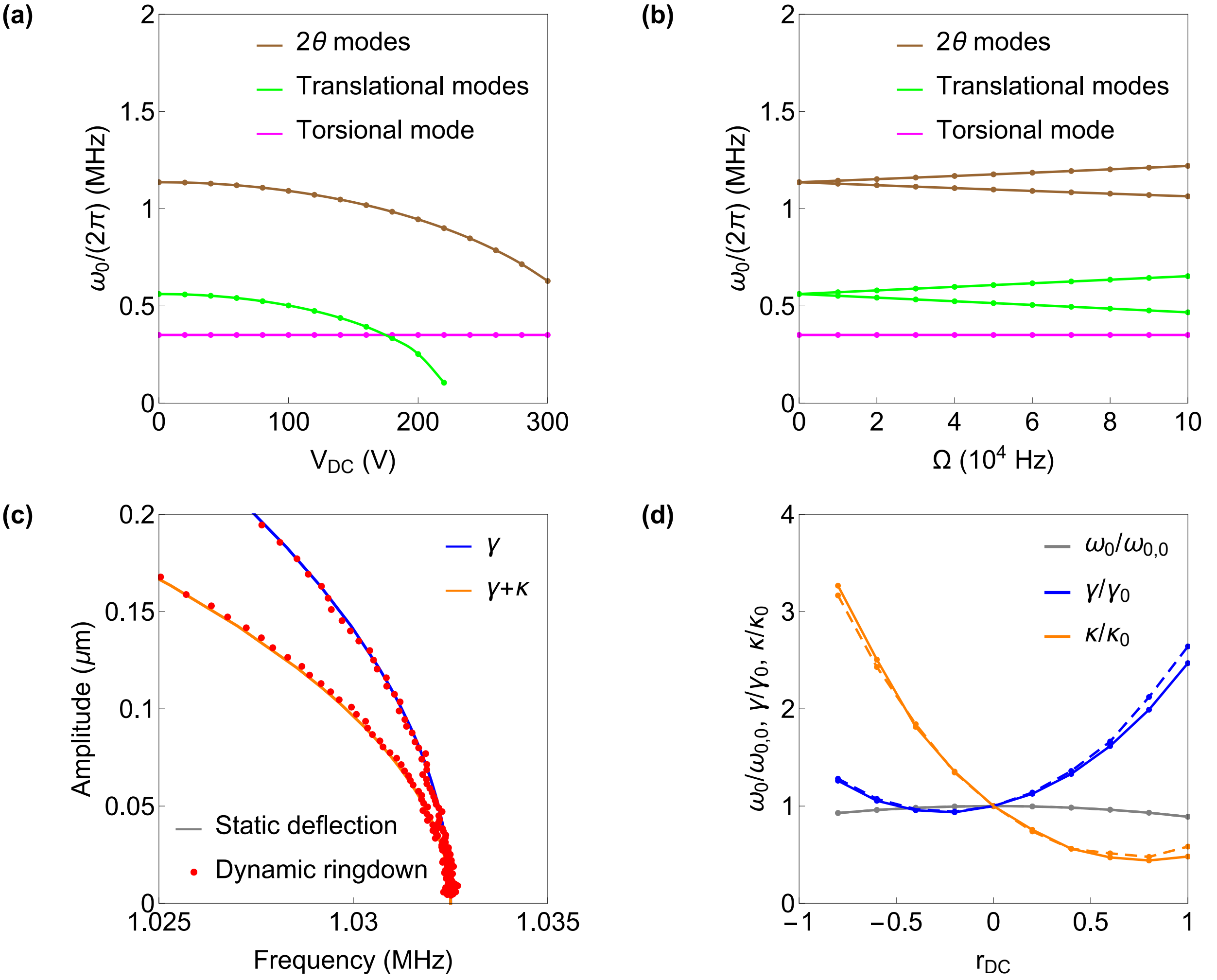

Fig. 4: COMSOL characterization results. **(a)** Changes in eigenfrequencies as the uniform DC bias voltage is increased for a non-rotating gyroscope, that is, for $r_{\mathrm{DC}} = 0$ and $\Omega = 0$. Electrostatic buckling can occur for the translational modes, indicated by an eigenfrequency going to zero. **(b)** Changes in eigenfrequencies as the angular rate Ω is increased, for zero DC bias on all electrodes, that is, for $V_{\mathrm{DC}} = 0$. Splitting of the degenerate modes occurs as the angular rate is increased. Note that the range of rotation rates shown far exceeds that used for sensing. For (a) and (b): the magenta curves represent the torsional mode, the green curves represent the translational modes, and the brown curves represent the drive and sense modes (2θ modes). **(c)** Comparison of the two characterization methods, with $r_{\mathrm{DC}} = 0$, $V_{\mathrm{DC}} = 150\,\mathrm{V}$, and $\Omega = 0$. Solid curves represent static deflection characterization, and the red dots represent ringdown response characterization. The blue curve indicates the Duffing effect (γ) and the orange curve indicates the sum of the dispersive coupling and Duffing effects ($\gamma + \kappa$). **(d)** Characterization results versus DC bias nonuniformity r_{DC} using static deflection (dashed curves) and ringdown response (solid curves), with $V_{\mathrm{DC}} = 150\,\mathrm{V}$ and $\Omega = 0$. Eigenfrequency is shown in gray, Duffing coefficient in blue, and dispersive coupling strength in orange. Data are normalized by the corresponding values for uniform DC bias. It can be seen from panels (c) and (d) that the results obtained using the two characterization methods are in excellent agreement

The characterization results for the two main nonlinear parameters, the Duffing coefficient γ and the dispersive coupling strength κ, are shown in Fig. 4c. The solid curves are created using the parameter values characterized by static deflection, serving as the backbone curve for the amplitude-dependent natural frequency, where the blue curve corresponds to $B = 0$ and the orange curve corresponds to $B = A$. The red dots illustrate data points of the instantaneous frequency computed during the ringdown process for $B(t) = 0$ and $B(t) = A(t)$, respectively. The ringdown responses track closely along the statically obtained backbone curves, indicating the that the static nonlinearities described by the potential U dominate the backbone curve. For $r_{\mathrm{DC}} = 0$, $V_{\mathrm{DC}} = 150\,\mathrm{V}$, and $\Omega = 0$, the coefficients for the ROM are $\omega_{0,0}/(2\pi) = 1.033\,\mathrm{MHz}$, $\gamma_0 = -13.83\,\mathrm{rad}^2/\mu\mathrm{m}^2\mu\mathrm{s}^2$, and $\kappa_0 = -14.97\,\mathrm{rad}^2/\mu\mathrm{m}^2\mu\mathrm{s}^2$.

Results for nonuniform DC bias are similarly obtained using both methods and are presented in Fig. 4d, where

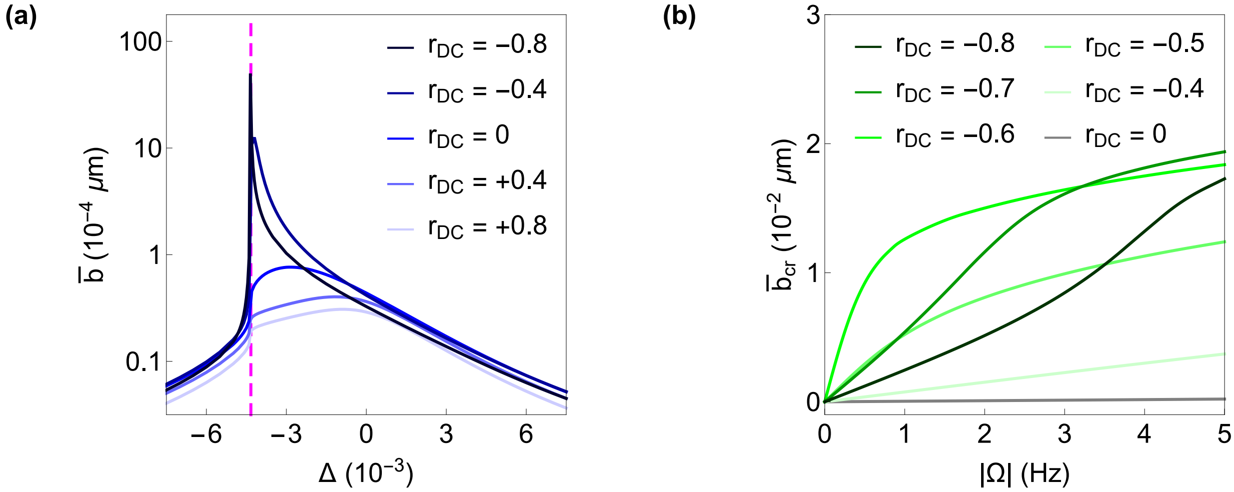

Fig. 5: Numerical simulation results using the ROM with $f = f_{\rm cr}$. **(a)** Sense mode amplitude versus frequency detuning parameter, with $\Omega = 1\,{\rm Hz}$. The blue, solid curves show the values of $\bar{b}$ for a variety of $r_{\rm DC}$ values, and the magenta dashed line indicates the detuning value corresponding to the critical drive frequency $\omega_{\rm cr}$. **(b)** Steady-state amplitude of the sense mode versus angular rate, with $\omega = \omega_{\rm cr}$. A significant improvement in the rate sensitivity is illustrated for the nonuniform DC bias tuning (green curves) in comparison to uniform DC bias (gray line, which does not even register an appreciable amplitude on the scale shown)

the value of $r_{\rm DC}$ ranges from -0.8 to $+1.0$, with an increment of 0.2. [3] As seen in the figure, by decreasing $r_{\rm DC}$ from zero, the Duffing nonlinearity is fairly unaffected while the dispersive coupling is strengthened, which is favorable to enhancing the gyroscope gain since it increases the intermodal parametric pumping without reducing the linear dynamic range. Furthermore, the fact that the two approaches have excellent agreement across this range of $r_{\rm DC}$ verifies the validity of the approaches and results for the nonuniform DC bias considered.

4.2 Optimization of S Using the ROM

For a system with weak damping and nonlinear coupling, the time to reach steady state can be orders of magnitude larger than the time constant suggested by the damping ratio. As a consequence, it is likely to be infeasible, or at least inconvenient, for a computational tool to simulate the system's steady state using the FE model, especially for a parameter study. Therefore, using the coefficients for the ROM determined by the characterization analysis described above allows for fast simulation of the system dynamics, and even theoretical analysis in some cases [40]. Of course, this must be checked with experiments, but the ROM is very useful for evaluating potential designs.

Fig. 5 shows a summary of numerical simulation results using the ROM with parameters obtained from COMSOL. Fig. 5a shows the sense mode steady-state amplitude in the frequency domain for harmonic excitation applied to the drive mode at the critical amplitude. The response curves are given for a variety of $r_{\rm DC}$ values from a set of simulations, plotted versus the nondimensional frequency detuning parameter $\Delta = \omega/\omega_0 - 1$. As displayed, the critical drive frequency yields the optimal sense mode amplitude for the system, which justifies the reason for its selection as the operating condition. Also, for Δ values near -0.8, however, the system may not be robust, in view of the narrow $-3\,{\rm dB}$ bandwidth, which is on the order of $10\,{\rm Hz}$, under which the phase noise of the drive mode must be circumscribed. It should be noted that at the critical amplitude the response of the drive mode is highly sensitive to fluctuations in the operating point, so if variations in the drive frequency (in open loop) or phase shift (in closed loop) are noticeable, a more robust operating point can be selected. Also, if operated in closed loop, no bistability occurs and it may be possible to operate well above this critical point.

The main results in the form of $b_{\rm cr}$ versus Ω, from which one determines S, are shown in Fig. 5b for a variety of pertinent $r_{\rm DC}$ values. These curves are determined using the critical excitation condition ($f = f_{\rm cr}$ and $\omega = \omega_{\rm cr}$) on the drive mode. The first thing to note about this set of curves is that the uniform DC bias, $r_{\rm DC} = 0$, represented by the gray curve, is nearly zero on the scale shown, indicating a very small value of the gain, given by the slope $S_0 = 4.24 \times 10^{-5}\,\mu{\rm m/Hz}$ near the origin. As clearly displayed, the green curves, representing different levels of nonuniform bias, generate a significant improvement in rate sensitivity compared to uniform bias. For instance,

---

[3] The results where $r_{\rm DC}$ is in the proximity of -1 are of no practical importance since the AC drive would be unable to operate the system.

$r_{\mathrm{DC}} = -0.6$ provides the largest gyroscope gain near $0\mathrm{Hz}$ rate, yet $r_{\mathrm{DC}} = -0.7$ gives a relatively large gyroscope gain while retaining a broader range of linear operation, that is, where the sensor input-output relationship is linear. Since it is oftentimes the sensor's linear range over Ω that is of interest in applications, one can select the optimal r_{DC} value that brings about the largest gain for a desired operating range of Ω. For example, using $r_{\mathrm{DC}} = -0.6$ improves the rate sensitivity by a factor of 500 for a range of Ω of 0–$0.3\,\mathrm{Hz}$, while $r_{\mathrm{DC}} = -0.7$ leads to an improvement by a factor of 120 for 0–$2.0\,\mathrm{Hz}$.

It is seen that by utilizing the nonuniform DC bias tuning strategy, the rate sensitivity can be dramatically improved solely from self-induced parametric amplification, which does not entail other complications in the system, e.g., additional control measures. Moreover, for a given device, one can vary the value of r_{DC} to tune the rate sensitivity and linear range based on the specifications of interest.

5 Conclusion

This paper considers a MEMS vibratory gyroscope and demonstrates significant improvements in the rate sensitivity by tuning its nonlinear characteristics using a specified pattern of nonuniform DC bias, as described by the parameter r_{DC}. Specifically, a COMSOL model is employed to characterize the system parameters, most importantly two nonlinear stiffness coefficients, for a range of r_{DC} values. Two methods of characterizing the nonlinearities are described, one using static deflection, which is favorable and fast with finite element computational tools, and the other uses dynamic ringdown response, which is often more convenient in experiments. To justify the ringdown response characterization, the amplitude-dependent natural frequency for a nonlinearly coupled two-mode system is defined and derived. The results show that the two characterization methods are in excellent agreement, thereby providing confidence for the subsequent numerical analysis using the ROM.

The large improvement in the angular rate sensitivity, by a factor of up to 500, is demonstrated using the nonuniform DC bias tuning. The results allow one to select the optimal r_{DC} value that leads to the largest gain for a desired range of operating angular rates Ω while maintaining sensor linearity. Consequently, this also allows the possibility of using a single sensor that can maintain the maximum rate sensitivity for multiple operating ranges, which is achieved by varying the corresponding r_{DC} accordingly.

The link between the FE model and the ROM requires knowledge about the desired dynamics of the device. In gyroscopes it is well known that the Coriolis coupling of the drive and sense modes is key, and that the Duffing nonlinearity imposes a limit on the operating amplitude, thus affecting the signal to noise ratio. More recently brought to light is the useful role of dispersive coupling between these modes, which enhances the input-output gain, and is exploited in the present study. These facts guide the form of the ROM and the coefficients of interest. This makes possible the connection between the FE model and the ROM.

It is important to note that there are many possible nonlinear coupling terms between eigenmodes of vibration. From the theory of normal forms it is known that most of these have inconsequential influence on the system response and, in fact, can be removed from the ROM using coordinate transformations [23]. For the present system it is known that dispersive coupling captures the essential effect, and it is distilled from the computational FE model using modal projections. The combination of computational tools with those from dynamical systems are just now gaining momentum and should pave the way for improved designs of mechanical and electro-mechanical systems that utilize and/or exploit nonlinearity [24, 57]. As they gain maturity, one should be able to incorporate other important effects in such nonlinear analyses, such as three dimensional effects, material anisotropy and nonlinearity, input-output transduction, and the ability to tune characteristics with shape optimization [24]. Along these lines, it will be important to be able to tune and optimize characteristics while enforcing certain constraints, for example, maintaining desired eigenfrequencies.

Appendix

A Parametric Amplification From Mode Coupling

In order to examine how the sense mode is parametrically amplified by the combined effects of the dispersive coupling and the Coriolis coupling, the generic equation of motion for a parametric amplifier [43, 44, 58] is introduced as

$$\ddot{q} + 2\zeta\omega_0\dot{q} + \omega_0^2\left(1 + \lambda\cos 2\omega t\right)q + \gamma q^3 = f\cos\left(\omega t + \psi\right), \tag{A.1}$$

where λ defines the nondimensional parametric pump level, and ψ describes the relative phase between the two drives. This equation is to be compared with the equation governing the sense mode dynamics. A notable feature of parametrically pumped systems is that one operates below the parametric instability threshold, so that a linear model can be used to predict the response. This instability threshold, commonly known as the Arnold tongue, when expressed in terms of a critical pump amplitude, is given by

$$\lambda_{\mathrm{AT}} = 4\sqrt{\zeta^2 + \Delta^2}, \tag{A.2}$$

where Δ is the nondimensional frequency detuning parameter defined in Sect. 2.

Moreover, with the drive mode response A replaced by $a\cos(\omega t + \phi)$, the two coupling terms (linear and nonlinear) in Eq. (3) can be rewritten as

$$-\frac{8}{5}\Omega\dot{A} = \frac{8}{5}\left|\Omega\right|\omega a\cos\left[\omega t + \phi - \frac{\pi}{2}\operatorname{sgn}(\Omega)\right], \tag{A.3}$$

$$\kappa A^2 B = \frac{1}{2}\kappa a^2 B + \frac{1}{2}\left|\kappa\right| a^2 B\cos 2\left[\omega t + \phi + \frac{\pi}{4} - \frac{\pi}{4}\operatorname{sgn}(\kappa)\right]. \tag{A.4}$$

By comparing these expressions to the generic form given in Eq. (A.1), the nondimensionalized eigenfrequency shift, the effective parametric pump level, the effective direct drive amplitude, and the relative phase can be acquired for use in Eq. (A.1). These parameters are given by

$$\Delta_{\mathrm{s}} = \frac{\kappa a^2}{4\omega_0^2}, \tag{A.5}$$

$$\lambda_{\mathrm{eff}} = \frac{\left|\kappa\right| a^2}{2\omega_0^2}, \tag{A.6}$$

$$f_{\mathrm{eff}} = \frac{8\left|\Omega\right|\omega a}{5}, \tag{A.7}$$

$$\psi = \left[\frac{1}{4}\operatorname{sgn}(\kappa) - \frac{1}{2}\operatorname{sgn}(\Omega) - \frac{1}{4}\right]\pi + 2n\pi. \tag{A.8}$$

It can be seen that the dispersive coupling engenders a softening effect on the eigenfrequency. The expressions also shed light on how the dispersive coupling corresponds to parametric pumping and how the Coriolis effect relates to direct excitation. A phase difference of $n\pi/2$ suggests a relative phase that gives rise to an amplifying effect [58].

Finally, to examine the amplifying effect in light of the self-induced parametric amplification, a nondimensional parameter η, which characterizes the relative parametric pumping strength, is introduced as

$$\eta = \frac{\lambda_{\mathrm{eff}}}{\lambda_{\mathrm{AT}}}. \tag{A.9}$$

As parameters are varied, if η approaches 1, the sense mode amplitude increases rapidly (conforming to the growth associated with approaching the parametric instability), and the effective parametric gain is salient (on the order of $(1-\eta)^{-1}$), thereby significantly amplification of the sense mode. The values of η in the frequency domain are shown in Fig. A.1a for a variety of r_{DC} values, and the results are consistent with those shown in Fig. 5a, where the critical drive frequency corresponds to the optimal gain for the system.

The parametric amplification at the critical drive parameters condition is obtained using $\Delta_{\mathrm{eff}} = \Delta_{\mathrm{cr}} - \Delta_{\mathrm{s,cr}}$ and $\bar{a} = \bar{a}_{\mathrm{cr}}$ in Eq. (A.2) and Eq. (A.6) respectively, after which Eq. (A.9) simplifies to a pumping strength ratio of

$$\eta_{\mathrm{cr}} = \frac{1}{\sqrt{3\left(3\frac{\gamma}{\kappa} - 1\right)^2 + 1}}. \tag{A.10}$$

This demonstrates that η_{cr} depends only on the ratio of the two nonlinear parameters γ/κ, and that it has a maximum value of 1 when $3\gamma = \kappa$. This condition renders the most favorable tuning of the nonlinearities, in which case the effective parametric pump level, in theory, reaches its threshold value. In terms of the nonuniform DC bias, Fig. A.1b illustrates how η depends on r_{DC} when the system is operating at the critical condition. This shows that the simplified analysis described here provides a good guide to what is observed in simulations of the two mode model.

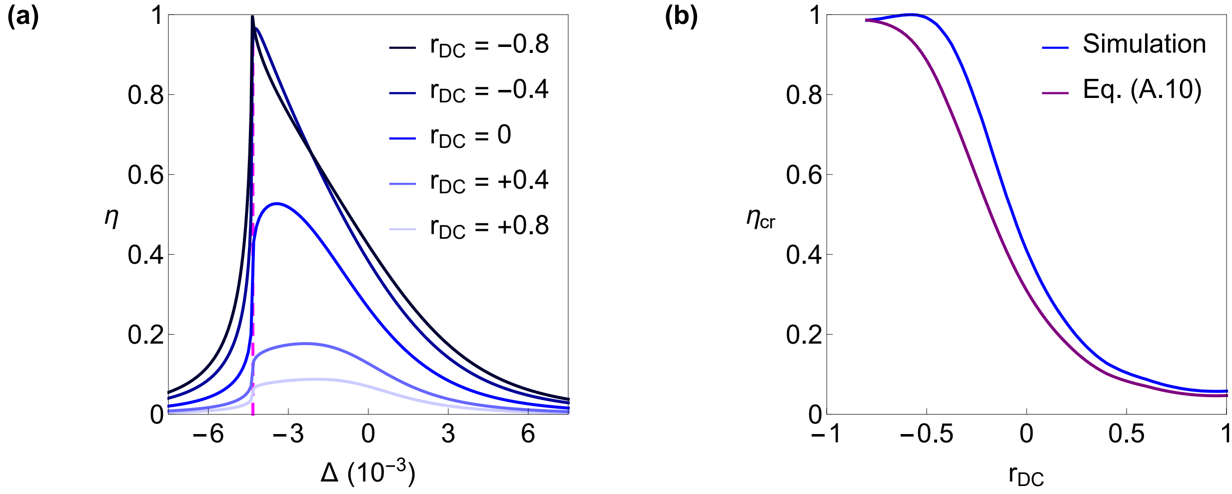

Fig. A.1: Self-induced parametric amplification with $f = f_{\mathrm{cr}}$. **(a)** Relative parametric pumping strength versus frequency detuning parameter, with $\Omega = 1\,\mathrm{Hz}$. The blue, solid curves show the values of η for a variety of r_{DC} values, and the magenta dashed line indicates the detuning value corresponding to the critical drive frequency ω_{cr}. **(b)** Relative parametric pumping strength versus DC bias nonuniformity parameter, with $\omega = \omega_{\mathrm{cr}}$ and $f = f_{\mathrm{cr}}$. It can be seen that η_{cr} has favorable values for r_{DC} between -0.8 and -0.4, from which the optimal DC bias tuning can be selected based on the desired linear operating range of the angular rate

B Derivation of the Amplitude-Dependent Natural Frequency

The dynamic ringdown response analysis for this coupled two-mode system requires the introduction of an amplitude-dependent natural frequency that is valid when both modes are active. In the following derivation, the relationship of $B(t) = \beta A(t)$ is assumed, where β is a constant, implying that the amplitudes of the two modes maintain a constant ratio and the phases are kept equal. That this relationship can be achieved for $\beta = 0$ and $\beta = 1$ is evinced by the aforementioned discussions in Sect. 3.2, although dynamic stability was not considered. Fortunately, the existence and stability of these constrained responses are verified by COMSOL. Moreover, this requirement can be fulfilled for an arbitrary β if $\gamma = \kappa$, which holds for uniform DC bias ($r_{\mathrm{DC}} = 0$), yet the result may also be able to provide a sensible approximation for other cases. Additionally, the system is assumed to undergo a ringdown process with slowly varying amplitude and phase, which occurs when the damping ratio is small, the system is unforced, and the spin rate is zero.

For Eq. (1), we substitute the stiffness coefficients $\omega_4 = \omega_5 = \omega_0$ and $\gamma_4 = \gamma_5 = \gamma$, and we impose the constraint $B = \beta A$. The constrained potential energy is then simplified to

$$U_{\mathrm{c}}(A) = \frac{1}{2}\omega_0^2\left(1+\beta^2\right)A^2 + \frac{1}{4}\gamma\left(1+\beta^4\right)A^4 + \frac{1}{2}\kappa\beta^2A^4. \tag{B.1}$$

The total constrained energy can thus be taken at the maximum displacement $|A|_{\max} = a$, namely, $E_{\mathrm{c}} = U_{\mathrm{c}}(a)$. The total constrained kinetic energy $\dot{A}^2/2 + \dot{B}^2/2$, therefore, is equal to $E_{\mathrm{c}} - U_{\mathrm{c}}$, which can be rewritten as

$$\frac{1}{2}\left(1+\beta^2\right)\left(\frac{dA}{dt}\right)^2 = E_{\mathrm{c}} - U_{\mathrm{c}}(A). \tag{B.2}$$

This naturally leads to an integral that determines the period of oscillation,

$$\tau = 4\int_0^a \sqrt{\frac{1+\beta^2}{2\left[E_{\mathrm{c}} - U_{\mathrm{c}}(A)\right]}}\,dA = 4\sqrt{2\xi}K\left(2\omega_0^2\xi - 1\right), \tag{B.3}$$

with

$$\xi = \frac{1+\beta^2}{\left[\left(1+\beta^4\right)\gamma + 2\beta^2\kappa\right]a^2 + 2\left(1+\beta^2\right)\omega_0^2}, \tag{B.4}$$

where $K(k)$ is the complete elliptic integral of the first kind. A Taylor series expansion is then used to obtain the amplitude-dependent natural frequency

$$\omega_{0,\mathrm{NL}} = \omega_0 + \frac{3\left[\left(1+\beta^4\right)\gamma + 2\beta^2\kappa\right]}{8\left(1+\beta^2\right)\omega_0}a^2. \tag{B.5}$$

In Sect. 3.2, the values $\beta = 0$ and $\beta = 1$ are taken successively to characterize γ and $\gamma + \kappa$ respectively.

Authors' Contributions

S. W. Shaw and P. M. Polunin conceived the problem. D. Li carried out the computational and theoretical analyses. S. W. Shaw guided the project. All authors were involved in drafting the paper.

Acknowledgements

This work has been supported in part by NSF grants No. CMMI-1662619 and No. CMMI-1561829, BSF grant 2018041, and by Florida Institute of Technology.

References

[1] A. N. Cleland. *Foundations of Nanomechanics*. Springer Science+Business Media, Berlin, 2003.

[2] M. I. Younis. *MEMS Linear and Nonlinear Statics and Dynamics*. Springer Science+Business Media, Berlin, 2011.

[3] V. Kaajakari. *Practical MEMS*. Small Gear Publishing, Las Vegas, 2009.

[4] J. F. Rhoads, S. W. Shaw, and K. L. Turner. Nonlinear dynamics and its applications in micro- and nanoresonators. *J. Dyn. Syst., Meas., Control*, 132:034001, 2010.

[5] O. Shoshani and S. W. Shaw. Resonant modal interactions in micro/nano-mechanical structures. *Nonlinear Dynamics*, pages 1–28, 2021.

[6] B. Andò, S. Baglio, C. Trigona, N. Dumas, L. Latorre, et al. Nonlinear mechanism in mems devices for energy harvesting applications. *J. Micromech. Microeng.*, 20:125020, 2010.

[7] R. L. Harne and K. W. Wang. A bifurcation-based coupled linear-bistable system for microscale mass sensing. *J. Sound Vib.*, 333(8):2241–2252, 2014.

[8] M. H. Hasan, F. M. Alsaleem, and H. M. Ouakad. Novel threshold pressure sensors based on nonlinear dynamics of mems resonators. *J. Micromech. Microeng.*, 28:065007, 2018.

[9] V. C. Meesala, M. R. Hajj, and E. Abdel-Rahman. Bifurcation-based mems mass sensors. *Int. J. Mech. Sci.*, 180:105705, 2020.

[10] A. Bouchaala, N. Jaber, O. Yassine, O. Shekhah, V. Chernikova, et al. Nonlinear-based mems sensors and active switches for gas detection. *Sensors*, 16(6):758, 2016.

[11] N. J. Miller, S. W. Shaw, and M. I. Dykman. Suppressing frequency fluctuations of self-sustained vibrations in underdamped nonlinear resonators. *Phys. Rev. Appl.*, 15:014024, 2021.

[12] C. Chen, D. H. Zanette, D. A. Czaplewski, S. Shaw, and D. López. Direct observation of coherent energy transfer in nonlinear micromechanical oscillators. *Nat. Commun.*, 8:15523, 2017.

[13] D. A. Czaplewski, C. Chen, D. López, O. Shoshani, A. M. Eriksson, et al. Bifurcation generated mechanical frequency comb. *Phys. Rev. Lett.*, 121:244302, 2018.

[14] D. A. Czaplewski, S. Strachan, O. Shoshani, S. W. Shaw, and D. López. Bifurcation diagram and dynamic response of a mems resonator with a 1:3 internal resonance. *Appl. Phys. Lett.*, 114:254104, 2019.

[15] D. Antonio, D. H. Zanette, and D. López. Frequency stabilization in nonlinear micromechanical oscillators. *Nature communications*, 3(1):1–6, 2012.

[16] G. Sobreviela, C. Zhao, M. Pandit, C. Do, S. Du, et al. Parametric noise reduction in a high-order nonlinear mems resonator utilizing its bifurcation points. *J. Microelectromech. Syst.*, 26(6):1189–1195, 2017.

[17] C. Zhao, G. Sobreviela, M. Pandit, S. Du, X. Zou, et al. Experimental observation of noise reduction in weakly coupled nonlinear mems resonators. *J. Microelectromech. Syst.*, 26(6):1196–1203, 2017.

[18] A. Uranga, G. Sobreviela, M. Riverola, F. Torres, and N. Barniol. Phase-noise reduction in a cmos-mems oscillator under nonlinear mems operation. *IEEE Trans. Circuits Syst. I Regul. Pap.*, 64(12):3047–3055, 2017.

[19] A. Z. Hajjaj, M. A. Hafiz, and M. I. Younis. Mode coupling and nonlinear resonances of mems arch resonators for bandpass filters. *Sci. Rep.*, 7:41820, 2017.

[20] O. Shoshani, M. I. Dykman, and S. W. Shaw. Tuning linear and nonlinear characteristics of a resonator via nonlinear interaction with a secondary resonator. *Nonlinear Dyn.*, 99:433–443, 2020.

[21] A. Givois, A. Grolet, O. Thomas, and J.-F. Deü. On the frequency response computation of geometrically nonlinear flat structures using reduced-order finite element models. *Nonlinear Dyn.*, 97:1747—-1781, 2019.

[22] V. Zega, G. Gattere, S. Koppaka, A. Alter, G. D. Vukasin, et al. Numerical modelling of non-linearities in mems resonators. *J. Microelectromech. Syst.*, 29(6):1443–1454, 2020.

[23] J. Guckenheimer and P. J. Holmes. *Nonlinear Oscillations, Dynamical Systems, and Bifurcations of Vector Fields*, volume 42. Springer Science+Business Media, Berlin, 2013.

[24] S. Dou, B. S. Strachan, S. W. Shaw, and J. S. Jensen. Structural optimization for nonlinear dynamic response. *Phil. Trans. R. Soc. A*, 373:20140408, 2015.

[25] L. L. Li, P. M. Polunin, S. Dou, O. Shoshani, B. S. Strachan, et al. Tailoring the nonlinear response of mems resonators using shape optimization. *Appl. Phys. Lett.*, 110:081902, 2017.

[26] F. Ayazi and K. Najafi. A harpss polysilicon vibrating ring gyroscope. *J. Microelectromech. Syst.*, 10(2):169–179, 2001.

[27] C. Acar and A. Shkel. *MEMS Vibratory Gyroscopes: Structural Approaches to Improve Robustness*. Springer Science+Business Media, New York, 2009.

[28] P. Minotti, A. Dellea, G. Mussi, A. Bonfanti, S. Facchinetti, et al. High scale-factor stability frequency-modulated mems gyroscope: 3-axis sensor and integrated electronics design. *IEEE Trans. Ind. Electron.*, 65(6):5040–5050, 2018.

[29] H. Yang, B. Zhou, L. Wang, H. Xing, and R. Zhang. A novel tri-axial mems gyroscope calibration method over a full temperature range. *Sensors*, 18(9):3004, 2018.

[30] H. Cao, H. Li, X. Shao, Z. Liu, Z. Kou, et al. Sensing mode coupling analysis for dual-mass mems gyroscope and bandwidth expansion within wide-temperature range. *Mech. Syst. Signal Process*, 98:448–464, 2018.

[31] K. Lu, X. Zhou, Q. Li, X. Wu, and D. Xiao. Coherent phonon manipulation in a disk resonator gyroscope with internal resonance. In *2020 IEEE International Symposium on Inertial Sensors and Systems (INERTIAL)*, pages 1–4, 2020.

[32] T.-H. Su, S. H. Nitzan, P. Taheri-Tehrani, and M. H. Kline. Silicon mems disk resonator gyroscope with an integrated cmos analog front-end. *IEEE Sens. J.*, 14(10):3426–3432, 2014.

[33] W. O. Davis, O. M. O'Reilly, and A. P. Pisano. On the nonlinear dynamics of tether suspensions for mems. *J. Vib. Acoust.*, 126 (3):326–331, 2004.

[34] A. Sarrafan, S. Azimi, F. Golnaraghi, and B. Bahreyni. A nonlinear rate microsensor utilising internal resonance. *Sci. Rep.*, 9: 8648, 2019.

[35] A. Tripathi and A. K. Bajaj. Design for 1:2 internal resonances in in-plane vibrations of plates with hyperelastic materials. *J. Vib. Acoust.*, 136:061005, 2014.

[36] B. J. Olson, S. W. Shaw, C. Shi, C. Pierre, and R. G. Parker. Circulant matrices and their application to vibration analysis. *Applied Mechanics Reviews*, 66(4), 2014.

[37] S. H. Nitzan, V. Zega, M. Li, C. H. Ahn, A. Corigliano, et al. Self-induced parametric amplification arising from nonlinear elastic coupling in a micromechanical resonating disk gyroscope. *Sci. Rep.*, 5:09036, 2015.

[38] X. Zhou, C. Zhao, D. Xiao, J. Sun, G. Sobreviela, et al. Dynamic modulation of modal coupling in microelectromechanical gyroscopic ring resonators. *Nat. Commun.*, 10:4980, 2019.

[39] P. M. Polunin. *Nonlinearities and noise in micromechanical resonators: from understanding to characterization and design tools*. PhD thesis, Michigan State University, East Lansing, MI, 2016.

[40] P. M. Polunin and S. W. Shaw. Self-induced parametric amplification in ring resonating gyroscopes. *Int. J. Nonlin. Mech.*, 94: 300–308, 2017.

[41] COMSOL Inc. Comsol multiphysics. Stockholm, Sweden, 2020, URL `www.comsol.com`.

[42] V. Zega, G. Gattere, S. Koppaka, A. Alter, G. D. Vukasin, et al. A unified epi-seal process for fabrication of high-stability microelectromechanical devices. *J. Microelectromech. Syst.*, 25(3):489–497, 2016.

[43] D. Rugar and P. Grütter. Mechanical parametric amplification and thermomechanical noise squeezing. *Phys. Rev. Lett.*, 67(6): 699–702, 1991.

[44] J. F. Rhoads and S. W. Shaw. The impact of nonlinearity on degenerate parametric amplifiers. *Appl. Phys. Lett.*, 96:234101, 2010.

[45] S. W. Shaw, O. Shoshani, and P. M. Polunin. *Modeling for nonlinear vibrational response of mechanical systems*, volume 570, pages 277–319. Springer, 09 2017. ISBN 978-3-319-40255-0.

[46] V. Denis, M. Jossic, C. Giraud-Audine, B. Chomette, A. Renault, et al. Identication of nonlinear modes using phase-locked-loop experimental continuation and normal form. *Mech. Syst. Signal Process.*, 106:430–452, 2018.

[47] A. Givois, J.-J. Tan, C. Touzé, and O. Thomas. Backbone curves of coupled cubic oscillators in one-to-one internal resonance: bifurcation scenario, measurements and parameter identification. *Meccanica*, 55(3):481–503, 2020.

[48] M. L. James, D. D. Shin, H.-K. Kwon, S. W. Shaw, and T. W. Kenny. Phase control of self-excited parametric resonators. *Phys. Rev. Appl.*, 12:044053, 2019.

[49] M. I. McEwan, J. R. Wright, J. E. Cooper, and A. Y. T. Leung. A finite element/modal technique for nonlinear plate and stiffened panel response prediction. In *19th AIAA Applied Aerodynamics Conference*, page 1595, 2001.

[50] A. Frangi and G. Gobat. Reduced order modelling of the non-linear stiffness in mems resonators. *Int. J. Non-Linear Mech.*, 116:211–218, 2019.

[51] C. Touzé, A. Vizzaccaro, and O. Thomas. Model order reduction methods for geometrically nonlinear structures: a review of nonlinear techniques. *Nonlinear Dyn.*, 105:1141–1190, 2021.

[52] J. J. Hollkamp and R. W. Gordon. Reduced-order models for nonlinear response prediction: Implicit condensation and expansion. *J. Sound Vib.*, 318(4–5):1139–1153, 2008.

[53] P. M. Polunin, Y. Yang, M. I. Dykman, T. W. Kenny, and S. W. Shaw. Characterization of mems resonator nonlinearities using the ringdown response. *J. Microelectromech. Syst.*, 25(2):297–303, 2016.

[54] M. Peeters, G. Kerschen, and J. C. Golinval. Dynamic testing of nonlinear vibrating structures using nonlinear normal modes. *J. Sound Vib.*, 330(3):486–509, 2011.

[55] S. Schein and R. T. M'Closkey. Parametric model identification of axisymmetric mems resonators. *Journal of Microelectromechanical Systems*, pages 1–13, 2021.

[56] S. W. Shaw and C. Pierre. Normal modes for non-linear vibratory systems. *J. Sound Vib.*, 164(1):85–124, 1993.

[57] O. Bayram, O. M. O'Reilly, and X. Zhou. On forced oscillations of a simple model for a novel wave energy converter. *Nonlinear Dyn.*, 67:1135–1146, 2012.

[58] D. Li and S. W. Shaw. The effects of nonlinear damping on degenerate parametric amplification. *Nonlinear Dyn.*, 102: 2433–2452, 2020.